Characterization of Excited States in a Multiple-Resonance-Type Thermally Activated Delayed Fluorescence Molecule Using Time-resolved Infrared Spectroscopy

Yuushi Shimoda, [1] Masaki Saigo, [1] Tomohiro Ryu, [1] Takumi Ehara, [1] Kiyoshi Miyata, [1] and Ken Onda*[1]

[1]Department of Chemistry, Kyushu University, 744 Motooka, Nishi, Fukuoka 829-0395

E-mail: konda@chem.kyushu-univ.jp

Abstract

We have investigated the correlation between the photophysical properties and the excited-state detailed characteristics in a multiple-resonance-type thermally activated delayed fluorescence (TADF) molecule, DABNA-1, using time-resolved infrared vibrational spectroscopy. In comparison of the distinctive vibrational spectra in the fingerprint region, 1000 - 1700 cm^{-1}, to the simulated spectra by density functional theory calculations, we found the best calculation condition. On the basis of the calculations, we determined the excited-state geometries and molecular orbitals of the lowest excited singlet (S_1) and triplet (T_1) states as well as the ground state (S_0). We revealed that the similarity of the potential surfaces between T_1 and S_0 suppresses the nonradiative decay and causes the high fluorescence quantum yield via TADF process.

Introduction

Thermally activated delayed fluorescence (TADF) molecules received tremendous attention due to their unique ability to improve the efficiency of organic light-emitting diodes (OLEDs)[1–5]. TADF molecules can convert excitons in the lowest triplet state (T_1) to the lowest singlet excited state (S_1) via reverse intersystem crossing (RISC) driven by thermal excitation. To understand their detailed mechanism, a lot of experimental[6–9] and theoretical[10–12] studies have been performed. However, there are few spectroscopic data to be compared to the theoretical calculations besides the energy gap between S_1 and T_1 states (ΔE_{ST})[13,14]. Vibrational spectra in the wavenumber region less than 1700 cm^{-1}, called fingerprint region, varies distinctively to reflect molecular characters. Thus, they are one of the ideal spectroscopic data to compare theoretical calculations [15–17]. Because there are not many methods to characterize a molecule in excited states, time-resolved infrared vibrational spectroscopy (TR-IR) is a variable method to explore photo-excited processes such as TADF with a high temporal resolution (< 1 ps).

To achieve an efficient RISC process in the room temperature, ΔE_{ST} should be sufficiently small (<0.2 eV). The basic design strategy for obtaining small ΔE_{ST} is to separate the highest occupied molecular orbital (HOMO) from the lowest unoccupied molecular orbital (LUMO). Many TADF molecules achieve this HOMO and LUMO separation by connecting electron donor (D) and electron acceptor (A). However, D-A type TADF molecules exhibit broadband emission because they have a CT character in the excited states and a large structural fluctuation. This would become a problem to realize commercial products although they have high external quantum efficiency.

Recently, Hatakeyama's group proposed a novel approach to separate HOMO and LUMO utilizing multiple resonance (MR) effect[18–22]. 5,9-diphenyl-5,9-diaza-13b-boranaphtho[3,2,1-*de*]anthracene (DABNA-1, the inset in Figure 1) is the first such TADF moleucle[19]. This molecule contains a triphenyl-boron framework, and the neighboring phenyl group is connected through two nitrogen atoms. The multiple resonance effects of boron and nitrogen atoms make HOMO and LUMO significantly separate and ΔE_{ST} small ~0.2 eV [19]. Unlike typical D-A type TADF molecules, MR-type TADF molecules exhibit high EQE and narrowband emission due to more rigid molecular structure.

Many MR-type TADF molecules with high emission quantum yield and high color purity have been actively investigated and developed[23–31]. The sharp emission and large oscillator strength of these derivatives are expected from rigidity of structure due to multiple resonance effects. However, the experimental evidence of this is only the small Stokes shift (<25 nm)[19]. TADF activity is also expected to be modulated by molecular geometry dynamics[32,33]. Thus, more experimental and theoretical studies in the excited states are highly demanded.

Here, we have investigated the excited-state geometries and molecular orbitals in DABNA-1 using TR-IR in conjugation with density functional theory (DFT) calculations and time-dependent (TD-) DFT calculations. Using the same method, we reported the correlations between structural dynamics and TADF activities[34,35]. Because the results of TD-DFT calculations strongly depend on a choice of functionals[36], comparison to experimental data is essential. Thus, we evaluated the reliability of used functionals by comparing the calculated vibrational

spectra by (TD-)DFT to the observed vibrational spectra in the fingerprint region. And then we obtained the geometries and molecular orbitals by the calculations using the conditions including the functional which best reproduced the observed spectra. On the basis of these results, we discuss the correlation between the photophysical properties and the excited-state geometries and molecular orbitals.

Experimental

Sample Preparation

DABNA-1 was purchased from Lumitec, Inc. and used after purification. We prepared solutions of the purified molecules in dichloromethane (DCM) purchased from Kanto Kagaku.

Fourier transform infrared (FT-IR) spectroscopy

The infrared vibrational spectra in the ground state were recorded with an FT-IR spectrophotometer (Shimadzu, IRPrestige-21). The samples were measured in the KBr pellets, which were prepared by mixing the sample with KBr powder at a ratio of 1:100 and using a hydraulic press. KBr purchased from Kanto Kagaku.

Raman spectroscopy

The Raman spectra in the ground state were recorded with a microlaser Raman spectroscope (Horiba, LabRAM ARAMIS). The samples were measured in powder.

TR-IR spectroscopy

The experimental setup for the pump-probe type TR-IR measurements has been reported previously[37–39]. Briefly, a broadband mid-IR pulse for a probe light (pulse duration: 120 fs, bandwidth: 150 cm^{-1}, tunable range: 1000-4000 cm^{-1}) was generated by difference frequency generation (DFG) between signal and idler from an optical parametric amplifier (OPA) pumped by output of a Ti:sapphire regenerative amplifier. The pump pulse was obtained by an optical parametric oscillator (central wavelength: 440 nm, pulse duration: 3 ns) pumped by output of a nanosecond Nd:YAG laser (EKSPLA NL220). The time delay between the pump pulse and probe pulses was generated using a digital delay/pulse generator (Stanford Research Systems, DG645). The polarization angles of the pulse for the pump and probe pulses were set to the magic angle. The pump pulse fluence was approximately 1.27 mJ/cm^2. The sample solutions were continuously circulated through an IR cell equipped with BaF_2 windows with an optical path length of 0.1 mm. A probe pulse passed through the IR cell was dispersed by a 19 cm polychromator, followed by detected using a 64-channel mercury cadmium telluride (MCT) infrared detector array. The concentrations of the solutions were 5 mM. All measurements were conducted after 1-hour bubbling using N_2 gas.

Quantum chemical calculations.

Quantum chemical calculations based on the density functional theory (DFT) and time-dependent (TD-)DFT were performed using the *Gaussian 16, Rev. A01* package.[40] IR and Raman spectra were calculated after geometrical optimization of each electronic state. We adopted the three basis sets: 6-31g(d), 6-31g(d,p), and 6-311g(d) and the five hybrid functionals with different Hartree-Fock (HF) exchange percentage: O3LYP (12%), B3LYP (20%), PBE0 (25%), BMK (42%) and M062X (54%) functionals by reference to previous studies[19,23,24]. The solvent effect was examined using the polarizable continuum model (PCM) of a dichloromethane solution (dielectric constant: 8.93, DCM). The vibrational frequencies of the calculated spectra were appropriately scaled to take into account frequency shifts caused by anharmonicity. The scaling factors of 0.980, 0.975, 0.965, 0.970, and 0.965 were adopted for O3LYP, B3LYP, PBE0, BMK, and M062X functionals, respectively.

Results and discussion

The optimized geometry in the ground state was examined by DFT calculations in comparison to FT-IR and Raman spectra. Figure 1a (PBE0) and S1 (all functionals) show the FT-IR spectrum and calculated IR spectra of DABNA-1 for the five hybrid functionals described in the experimental section. The calculated IR spectra generally well reproduce the FT-IR spectrum, but the spectral patterns at 1550 - 1650 cm^{-1} for BMK and M062X do not match that of FT-IR spectrum. Figure 1b (PBE0) and S2 (all functionals) show the Raman spectrum and the calculated Raman spectra. The calculated Raman spectra are also well consistent with the observed Raman spectrum, but the patterns at 1000 - 1250 cm^{-1} for BMK and at 1500 - 1650 cm^{-1} for M062X are slightly different from those corresponding to the observed one. These results suggest that the O3LYP, B3LYP and PBE0 are more suitable for examining the optimized geometry in the ground state.

To assign the TR-IR spectra to the electronic excited states, we measured the temporal evolutions of the TR-IR spectra. Figure 2a shows TR-IR spectra up to 50 ns in a dichloromethane (DCM) solution at 1120 - 1240 cm^{-1} after photoexcitation. Both the transient absorption bands (upward) and bleach bands (downward) emerge immediately after photoexcitation

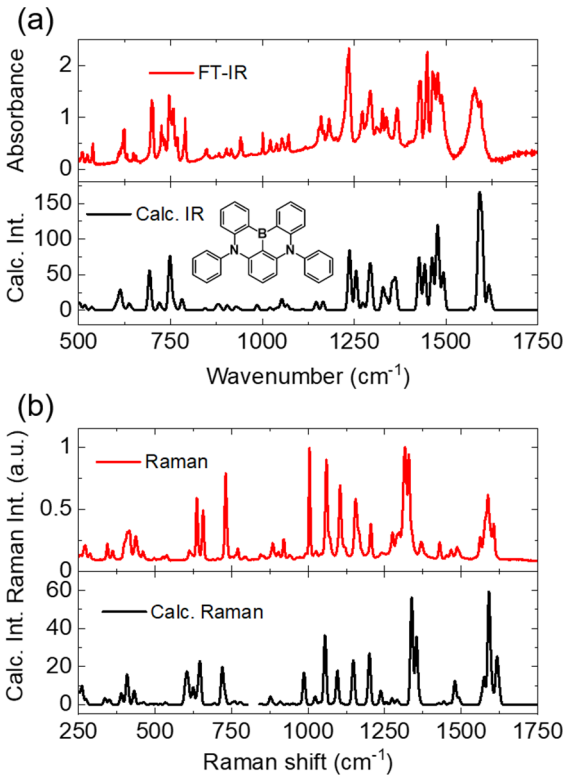

Figure 1. Comparison of the observed spectra (upper) and calculated vibrational spectra (lower) for (a) FT-IR and (b) Raman spectroscopy of DABNA-1. Calculated spectra were obtained using PBE0/6-31g(d,p). Solvent effect was taken into account using PCM for DCM. (Inset of a) Molecular structure of DABNA-1.

less than 1 ps. Black circles in Figure 2b represent the temporal profile of the transient absorption band at 1232 cm^{-1}. By fitting using an exponential function (red line in Figure 2b), we obtained a fast decay component ~7 ns and a component that would not change up to 50 ns (shown by dashed line in Figure 2b).

Considering that the decrease of the bleach bands corresponds to the recovery of the ground state population, the fast component is attributed to the deactivation process of S_1 to S_0 after photoexcitation, and this process is dominant compared to the intersystem crossing from S_1 to T_1. This result is consistent with the previous study; the main component of DABNA-1 emission is prompt fluorescence rather than delayed fluorescence[19]. Furthermore, the time constant ~ 7 ns is in good agreement with the prompt fluorescence lifetime ~9.5 ns previously reported[19].

The relatively minor component with a much longer time constant than 50 ns indicates that some population remains in an excited state even at 50 ns after the fast decay. Given that DABNA-1 has TADF activity, the remaining component after fluorescence lifetime is attributed to the transient vibrational absorption in the T_1 state. From these results, the TR-IR spectra at 1 ns and 50 ns are assigned to the vibrational spectra of the S_1 and T_1 states, respectively. The fact that the spectra are not drastically changed up to 50 ns as shown in Figure 2a and S3 indicates that the molecular geometry and electron distribution are not much changed along with intersystem crossing (ISC) from S_1 to T_1.

Figure 3 compares the TR-IR spectrum assigned to S_1 at 1 ns to the calculated difference IR spectra between the S_1 and S_0 states by TD-DFT calculations using the five functionals. The calculated spectra using BMK and M062X does not reproduce the band positions and shapes in the TR-IR spectrum in the whole wavenumber regions. The calculated spectrum using O3LYP is rather similar to the TR-IR spectrum

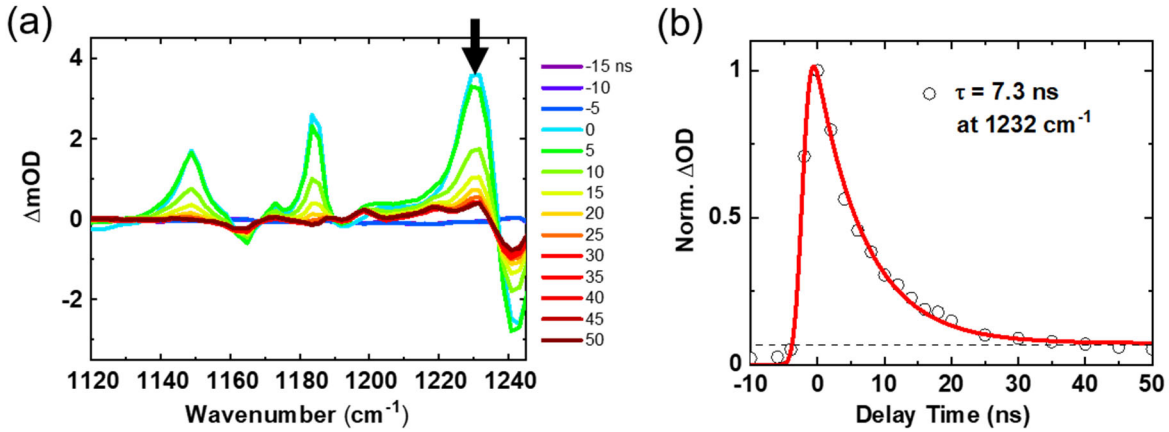

Figure 2. (a) Temporal evolutions of TR-IR spectra in DCM solution ranging from 1120 to 1240 cm^{-1} after photoexcitation with 440 nm. (b) Temporal profile at 1232 cm^{-1} (black circles) and fitting curve using an exponential function (red line)

but the spectral pattern at 1150 - 1250 cm^{-1} do not match each other. Compared to these calculated spectra, the spectra using B3LYP and PBE0 are in good agreement with the TR-IR spectrum in all wavenumber range.

Figure S4 compares the TR-IR spectrum at 50 ns to the calculated difference IR spectra between T_1 and S_0 states by DFT calculation using the five functionals. The calculated spectra using BMK and M062X in the T_1 state did not reproduce the spectral shape for the experimental spectrum in the region around 1200-1400 cm^{-1}, whereas the calculated spectra using PBE0 and B3LYP functional are in good agreement with the TR-IR spectrum. This trend is similar to that of the S_1 state although their calculation methods are different: TD-DFT for S_1 and DFT for T_1. Figure 4 compares the TR-IR spectra to the best agreed calculated spectra for the S_1 and T_1 states.

The B3LYP and PBE0 functionals are hybrid functional with HF exchange of 20-25%. These functionals have also been used in the previous reserches[19,23,24]. These experimental results support that HF exchange percent of 20-25% is suitable for examining the geometries in the excited states for MR type molecules. Besides, we confirmed the calculated spectra did not depend on the choice of basis set (Figure S5). Incorporation of the dielectric effect from a solvent using PCM showed trivial effects (Figure S6).

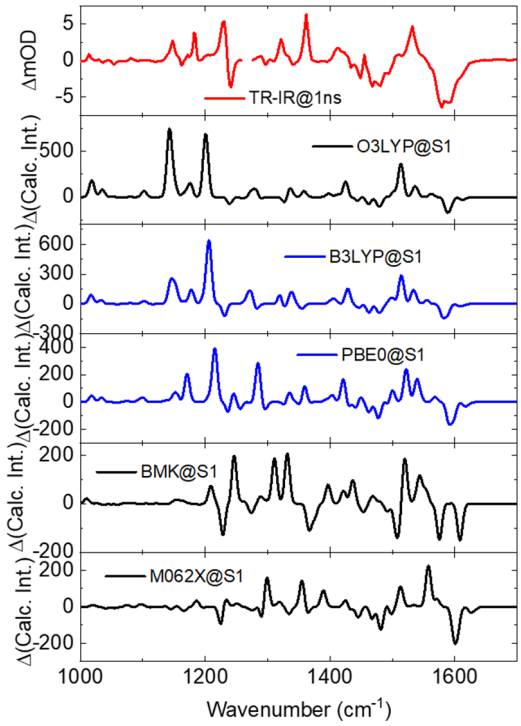

Figure 3. Dependence on the functional for calculated spectrum in the S_1 state. The basis set was 6-31g(d,p) and solvent effect was taken into account using PCM for DCM.

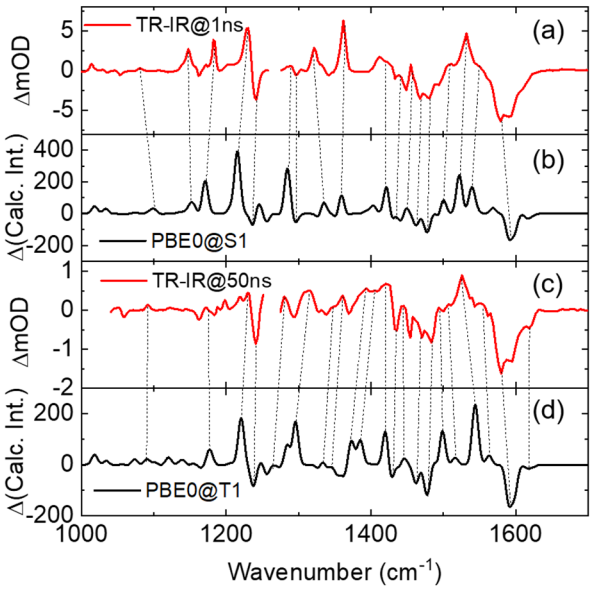

Figure 4. Comparison of (a,c) observed spectra and (b,d) calculated vibrational spectra for (a,b) S_1 and (c,d) T_1 states of DABNA-1. The range neighboring 1265 cm^{-1} could not be measured due to DCM solvent absorption. Calculated spectra were obtained using TD-DFT for S_1 state and DFT for T_1 with PBE0/6-31g(d,p). Solvent effect was taken into account using PCM for DCM.

We considered the detailed molecular structures in each electronic state on the basis of the calculations in the best agreement with the observed spectra. Figure 5 shows the optimized geometries in each state, and Table 1 shows structural parameters: bond lengths,

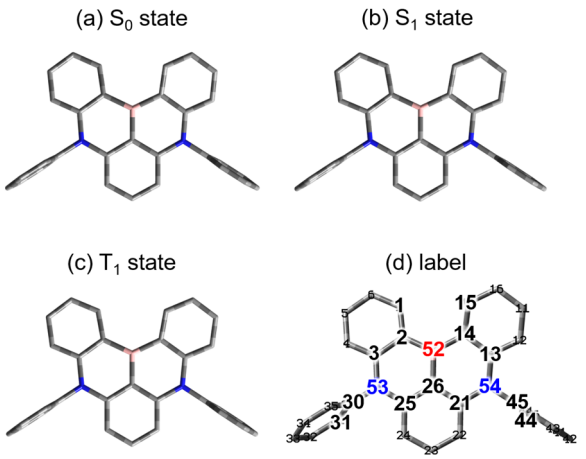

Figure 5. (a, b, c) Optimized structures for each state. Calculations were performed using TD-DFT for S_1 state and DFT for S_0 and T_1 state with PBE0/6-31g(d,p). Solvent effect was taken into account using PCM for DCM. (d) Atom labels. hydrogen atoms are omitted for clarity.

Table 1. Structural parameters with optimized geometries for S_0, S_1, and T_1 states. Calculations were performed using TD-DFT for S_1 state and DFT for S_0 and T_1 states with PBE0/6-31g(d,p). Solvent effect was taken into account using PCM for DCM. Atom labels are shown in Figure 5d

PBE0/6-31g(d,p)	S_0	S_1	T_1	$\Delta(S_1-S_0)$	$\Delta(T_1-S_0)$	$\Delta(T_1-S_0)/\Delta(S_1-S_0)$
			bond length			
B52-C2 (B52-C14)	1.5447	1.5376	1.5415	0.0072	0.0032	0.4463
B52-C26	1.5138	1.5283	1.5158	-0.0145	-0.0020	0.1387
N53-C3 (N54-C13)	1.3965	1.4093	1.4092	-0.0127	-0.0127	0.9992
N53-C25 (N54-C21)	1.3929	1.3867	1.3897	0.0062	0.0033	0.5217
C2-C3 (C13-C14)	1.4205	1.4338	1.4329	-0.0133	-0.0125	0.9355
C25-C26 (C21-C26)	1.4195	1.4059	1.4125	0.0136	0.0070	0.5181
N54-C45 (N53-C30)	1.4347	1.4368	1.4371	-0.0021	-0.0024	1.1635
C1-C15	3.3275	3.3622	3.3695	-0.0347	-0.0420	1.2114
			angle			
C2-B52-C14	129.369	129.959	129.937	-0.590	-0.569	0.964
C2-B52-C26 (C14-B52-C26)	115.316	115.021	115.031	0.295	0.284	0.964
C3-N53-C25 (C13-N54-C21)	123.971	124.525	124.387	-0.555	-0.416	0.751
C3-N53-C30 (C13-N54-C45)	118.303	117.575	117.724	0.728	0.579	0.795
			dihedral angle			
C1-C2-C14-C15	21.750	16.568	16.274	5.182	5.476	1.057
C3-N53-N54-C13	14.232	10.423	10.337	3.810	3.896	1.023
C3-N53-C30-C31 (C13-N54-C45-C44)	87.642	87.704	88.053	-0.062	-0.411	6.635

angles, and dihedral angles in each state. It was clarified that the diaza-boranaphtho-anthracene unit, which is the central scaffold of DABNA-1, mainly maintained its flatness in all states. As confirmed experimentally from the TR-IR spectra, the structural changes along with ISC are very small. These results are consistent with the previous report[19,23]. We confirmed the excited state geometries and its rigidity with the experimental evidence.

These structural features are entirely different from typical D-A type TADF molecules we already reported[34,35] in which the structural change is small in the excited state. This rigidity must bring about the high oscillator strength and a narrow FWHM with a small Stokes shift of DABNA-1. Table S1-S4 show the structural parameters obtained from the other functionals. While the results of B3LYP and PBE0 functionals show similar geometries, the results of the other functionals show a slight difference in the helical twisting of the main skeleton in the excited state.

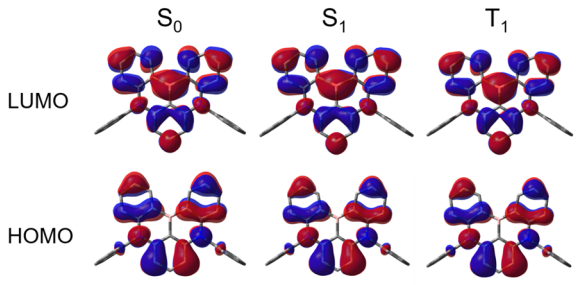

Figure 6. HOMO and LUMO in S_0, S_1, and T_1 states. Calculations were performed using TD-DFT for S_1 state and DFT for S_0 and T_1 state. The functional and basis set was PBE0 and 6-31g(d,p), respectively. Solvent effect was taken into account using PCM for DCM.

Although the main skeleton of DABNA-1 does not change drastically in the excited states, there is a slight difference in geometry between the ground and excited states. Focusing on the bond lengths neighboring the boron and nitrogen atoms, they are changed slightly in the excited states. As shown in Figure 6, the area where HOMO was distributed became longer in the excited states, and the area where LUMO was distributed became shorter in the excited states. These changes were caused by the change in the orbital distribution due to electronic excitation. Furthermore, focusing on the diaza-boranaphtho-anthracene unit, the helical twisting in the excited states was slightly relaxed than in the ground state. The distance between carbon atoms on the edges of the two phenazaborines (C1-C15 in Figure 5) increases, and the dihedral angle between the two phenazaborines decreases. This means that the skeleton becomes flatter in the excited states. The tendency of these slight structural changes is observed for the other functionals that reproduced the experimental spectra.

There is a very little but significant difference in geometry between the S_1 and T_1 states. We compare the amount of change in each structural parameter from the S_0 state to the S_1 and T_1 states. The normalized values of the variation from S_0 to S_1 and T_1 ($\Delta(T_1\text{-}S_0)/\Delta(S_1\text{-}S_0)$) were calculated and are shown in Table 1. If this value is less than unity for the most structural parameters, meaning that the geometry in the T_1 state was closer to that in the S_0 state than that in the S_1 state. This indicates that the potential surfaces of the S_0 and T_1 states are almost the same each other. In this case, the Franck-Condon factor for the nonradiative decay between the S_0 and T_1 states becomes very small, and the nonradiative process is highly suppressed (the energy gap law). A previous study reported that the lifetime of TADF for DABNA-1 was ~94 μs[19], which is consistent with this speculation.

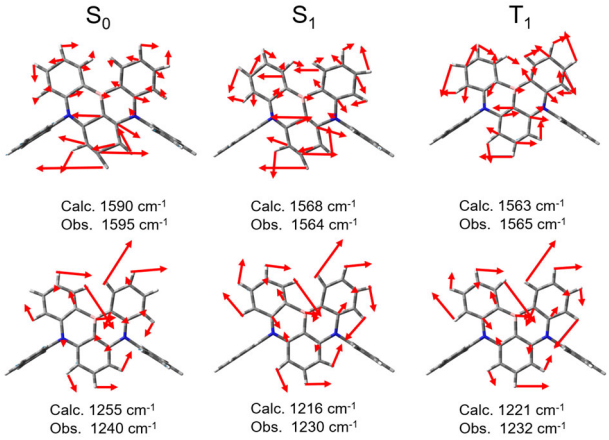

Figure 7. Comparison of vibrational modes of S_0, S_1, and T_1 states. Calculations were performed using TD-DFT for S_1 state and DFT for S_0 and T_1 state with PBE0/6-31g(d,p) level. Solvent effect was taken into account using PCM for DCM.

The bands are shifted in the TR-IR spectrum even though the geometries in the excited states are not changed drastically from the ground state. Because the structural change in the ground state and the excited states is suppressed, the normal vibrational mode should be the same in each state. We assigned the vibrational modes to some major peaks on the basis of the DFT calculations (Figure S7-9). It was revealed that most of the vibrational modes in the excited states were red-shifted than those in the ground state (Figure 7). This result indicates that the potential in the excited state is slightly shallower than that in the ground state, which causes the IR spectral change in the excited states.

Summary

We investigated the molecular geometries and molecular orbitals in the lowest singlet (S_1) and triplet (T_1) excited states as well as the ground state (S_0) in the TADF molecule using multiple resonance effects, DABNA-1, using FT-IR, Raman, and TR-IR spectroscopies. By comparing these spectra to the calculated spectra by DFT or TD-DFT calculations, we determined the best calculation condition. We found a little spectral change from the S_1 to T_1 states, indicating that the structural change along with intersystem crossing is very small. We carefully examine the difference in geometry between the states on the basis of the calculations, and found that similarity in vibrational potential between the S_0 and T_1 states causes the long lifetime and efficient TADF process of the T^1 state.

Acknowledgment

This work was supported in part by JSPS KAKENHI Grant Number JP17H06375, JP18H05170, and JP20H05106. The computations were performed using the Research Center for Computational Science (National Institute of Natural Sciences) and Research Institute for Information Technology (Kyushu University).

References

1 H. Uoyama, K. Goushi, K. Shizu, H. Nomura, C. Adachi, *Nature* **2012**, *492*, 234.
2 F. B. Dias, K. N. Bourdakos, V. Jankus, K. C. Moss, K. T. Kamtekar, V. Bhalla, J. Santos, M. R. Bryce, A. P. Monkman, *Advanced Materials* **2013**, *25*, 3707.
3 J. W. Sun, J. H. Lee, C. K. Moon, K. H. Kim, H. Shin, J. J. Kim, *Advanced Materials* **2014**, *26*, 5684.
4 S. Hirata, Y. Sakai, K. Masui, H. Tanaka, S. Y. Lee, H. Nomura, N. Nakamura, M. Yasumatsu, H. Nakanotani, Q. Zhang, K. Shizu, H. Miyazaki, C. Adachi, *Nature Materials* **2015**, *14*, 330.
5 H. Kaji, H. Suzuki, T. Fukushima, K. Shizu, K. Suzuki, S. Kubo, T. Komino, H. Oiwa, F. Suzuki, A. Wakamiya, Y. Murata, C. Adachi, *Nature Communications* **2015**, *6*, 1.
6 T. Hosokai, H. Matsuzaki, H. Nakanotani, K. Tokumaru, T. Tsutsui, A. Furube, K. Nasu, H. Nomura, M. Yahiro, C. Adachi, *Science Advances* **2017**, *3*, e1603282.
7 H. Noda, X. K. Chen, H. Nakanotani, T. Hosokai, M. Miyajima, N. Notsuka, Y. Kashima, J. L. Brédas, C. Adachi, *Nature Materials* **2019**, *18*, 1084.
8 T. Kobayashi, A. Niwa, K. Takaki, S. Haseyama, T. Nagase, K. Goushi, C. Adachi, H. Naito, *Physical Review Applied* **2017**, *7*, 1.

9 E. W. Evans, Y. Olivier, Y. Puttisong, W. K. Myers, T. J. H. Hele, S. M. Menke, T. H. Thomas, D. Credgington, D. Beljonne, R. H. Friend, N. C. Greenham, *Journal of Physical Chemistry Letters* **2018**, *9*, 4053.

10 X. K. Chen, D. Kim, J. L. Brédas, *Accounts of Chemical Research* **2018**, *51*, 2215.

11 M. K. Etherington, J. Gibson, H. F. Higginbotham, T. J. Penfold, A. P. Monkman, *Nature Communications* **2016**, *7*, 13680.

12 J. Gibson, A. P. Monkman, T. J. Penfold, *ChemPhysChem* **2016**, *17*, 2956.

13 S. Huang, Q. Zhang, Y. Shiota, T. Nakagawa, K. Kuwabara, K. Yoshizawa, C. Adachi, *Journal of Chemical Theory and Computation* **2013**, *9*, 3872.

14 X. K. Chen, S. F. Zhang, J. X. Fan, A. M. Ren, *Journal of Physical Chemistry C* **2015**, *119*, 9728.

15 J. Clarkson, W. E. Smith, *Journal of Molecular Structure* **2003**, *655*, 413.

16 N. Sundaraganesan, S. Ilakiamani, P. Subramani, B. D. Joshua, *Spectrochimica Acta - Part A: Molecular and Biomolecular Spectroscopy* **2007**, *67*, 628.

17 B. Klaumünzer, D. Kröner, P. Saalfrank, *Journal of Physical Chemistry B* **2010**, *114*, 10826.

18 H. Hirai, K. Nakajima, S. Nakatsuka, K. Shiren, J. Ni, S. Nomura, T. Ikuta, T. Hatakeyama, *Angewandte Chemie - International Edition* **2015**, *54*, 13581.

19 T. Hatakeyama, K. Shiren, K. Nakajima, S. Nomura, S. Nakatsuka, K. Kinoshita, J. Ni, Y. Ono, T. Ikuta, *Advanced Materials* **2016**, *28*, 2777.

20 Y. Kondo, K. Yoshiura, S. Kitera, H. Nishi, S. Oda, H. Gotoh, Y. Sasada, M. Yanai, T. Hatakeyama, *Nature Photonics* **2019**, *13*, 678.

21 N. Ikeda, S. Oda, R. Matsumoto, M. Yoshioka, D. Fukushima, K. Yoshiura, N. Yasuda, T. Hatakeyama, *Advanced Materials* **2020**, *32*, 1.

22 S. Oda, T. Hatakeyama, W. Kumano, T. Hama, R. Kawasumi, K. Yoshiura, *Angewandte Chemie* **2020**, 1.

23 L. Lin, J. Fan, L. Cai, C. K. Wang, *Molecular Physics* **2018**, *116*, 19.

24 T. Northey, T. J. Penfold, *Organic Electronics* **2018**, *59*, 45.

25 X. Liang, Z. P. Yan, H. B. Han, Z. G. Wu, Y. X. Zheng, H. Meng, J. L. Zuo, W. Huang, *Angewandte Chemie - International Edition* **2018**, *57*, 11316.

26 Y. Zhang, D. Zhang, J. Wei, Z. Liu, Y. Lu, L. Duan, *Angewandte Chemie* **2019**, *131*, 17068.

27 A. Pershin, D. Hall, V. Lemaur, J. C. Sancho-Garcia, L. Muccioli, E. Zysman-Colman, D. Beljonne, Y. Olivier, *Nature Communications* **2019**, *10*, 3.

28 S. M. Suresh, E. Duda, D. Hall, Z. Yao, S. Bagnich, A. M. Z. Slawin, H. Bässler, D. Beljonne, M. Buck, Y. Olivier, A. Köhler, E. Zysman-Colman, *Journal of the American Chemical Society* **2020**, *142*, 6588.

29 M. Yang, I. S. Park, T. Yasuda, *Journal of the American Chemical Society* **2020**, *142*, 19468.

30 D. Hall, S. M. Suresh, P. L. dos Santos, E. Duda, S. Bagnich, A. Pershin, P. Rajamalli, D. B. Cordes, A. M. Z. Slawin, D. Beljonne, A. Köhler, I. D. W. Samuel, Y. Olivier, E. Zysman-Colman, *Advanced Optical Materials* **2020**, *8*.

31 Y. Zhang, D. Zhang, J. Wei, X. Hong, Y. Lu, D. Hu, G. Li, Z. Liu, Y. Chen, L. Duan, *Angewandte Chemie* **2020**, *132*, 17652.

32 R. S. Nobuyasu, Z. Ren, G. C. Griffiths, A. S. Batsanov, P. Data, S. Yan, A. P. Monkman, M. R. Bryce, F. B. Dias, *Advanced Optical Materials* **2016**, *4*, 597.

33 T. J. Penfold, E. Gindensperger, C. Daniel, C. M. Marian, *Chemical Reviews* **2018**, *118*, 6975.

34 M. Saigo, K. Miyata, S. Tanaka, H. Nakanotani, C. Adachi, K. Onda, *Journal of Physical Chemistry Letters* **2019**, *10*, 2475.

35 Y. Shimoda, K. Miyata, M. Saigo, Y. Tsuchiya, C. Adachi, K. Onda, *Journal of Chemical Physics* **2020**, *153*, 204702.

36 D. Jacquemin, V. Wathelet, E. A. Perpète, C. Adamo, *Journal of Chemical Theory and Computation* **2009**, *5*, 2420.

37 N. Fukazawa, T. Tanaka, T. Ishikawa, Y. Okimoto, S. Koshihara, T. Yamamoto, M. Tamura, R. Kato, K. Onda, *The Journal of Physical Chemistry C* **2013**, *117*, 13187.

38 T. Mukuta, N. Fukazawa, K. Murata, A. Inagaki, M. Akita, S. Tanaka, S. Koshihara, K. Onda, *Inorganic Chemistry* **2014**, *53*, 2481.

39 T. Mukuta, S. Tanaka, A. Inagaki, S. Y. Koshihara, K. Onda, *ChemistrySelect* **2016**, *1*, 2802.

40 M. J. Frisch, G. W. Trucks, H. B. Schlegel, G. E. Scuseria, M. A. Robb, J. R. Cheeseman, G. Scalmani, V. Barone, G. A. Petersson, H. Nakatsuji, X. Li, M. Caricato, A. V. Marenich, J. Bloino, B. G. Janesko, R. Gomperts, B. Mennucci, H. P. Hratchian, J. V. Ortiz, A. F. Izmaylov, J. L. Sonnenberg, D. Williams-Young, F. Ding, F. Lipparini, F. Egidi, J. Goings, B. Peng, A. Petrone, T. Henderson, D. Ranasinghe, V. G. Zakrzewski, J. Gao, N. Rega, G. Zheng, W. Liang, M. Hada, M. Ehara, K. Toyota, R. Fukuda, J. Hasegawa, M. Ishida, T. Nakajima, Y. Honda, O. Kitao, H. Nakai, T. Vreven, K. Throssell, J. Montgomery, J. A., J. E. Peralta, F.

Ogliaro, M. J. Bearpark, J. J. Heyd, E. N. Brothers, K. N. Kudin, V. N. Staroverov, T. A. Keith, R. Kobayashi, J. Normand, K. Raghavachari, A. P. Rendell, J. C. Burant, S. S. Iyengar, J. Tomasi, M. Cossi, J. M. Millam, M. Klene, C. Adamo, R. Cammi, J. W. Ochterski, R. L. Martin, K. Morokuma, O. Farkas, J. B. Foresman, D. J. Fox, *Gaussian 16, Revision A.03,* Gaussian, Inc., Wallingford CT, **2016**.

Supporting Information

Characterization of Excited States in a Multiple-Resonance-Type Thermally Activated Delayed Fluorescence Molecule Using Time-resolved Infrared Spectroscopy

Yuushi Shimoda, [1] Masaki Saigo, [1] Tomohiro Ryu, [1] Takumi Ehara, [1] Kiyoshi Miyata, [1] and Ken Onda*[1]

[1]Department of Chemistry, Kyushu University, 744 Motooka, Nishi, Fukuoka 829-0395

E-mail: konda@chem.kyushu-univ.jp

Table of Contents

Table S1-S4

Figures S1 - 10

Table S1-S4

Table S1. The structural parameter with optimized structures for each state. Calculated using TD-DFT for S_1 state and DFT for S_0 and T_1 state with O3LYP/6-31g(d,p). Solvent effect was taken into account using PCM for DCM.

O3LYP/6-31g(d,p)	S_0	S_1	T_1	$\Delta(S_1-S_0)$	$\Delta(T_1-S_0)$	$\Delta(T_1-S_0)/\Delta(S_1-S_0)$
			bond length			
B52-C2 (B52-C14)	1.5492	1.5401	1.5460	0.0090	0.0032	0.3518
B52-C26	1.5170	1.5392	1.5191	-0.0222	-0.0021	0.0959
N53-C3 (N54-C13)	1.4027	1.4212	1.4123	-0.0185	-0.0096	0.5165
N53-C25 (N54-C21)	1.4002	1.3897	1.4010	0.0105	-0.0008	-0.0771
C2-C3 (C13-C14)	1.4263	1.4374	1.4391	-0.0111	-0.0128	1.1512
C25-C26 (C21-C26)	1.4249	1.4093	1.4183	0.0156	0.0066	0.4211
N54-C45 (N53-C30)	1.4419	1.4440	1.4442	-0.0021	-0.0022	1.0613
C1-C15	3.3576	3.3885	3.3914	-0.0309	-0.0338	1.0966
			angle			
C2-B52-C14	129.479	130.278	129.931	-0.800	-0.453	0.5660
C2-B52-C26 (C14-B52-C26)	115.261	114.861	115.034	0.400	0.226	0.5661
C3-N53-C25 (C13-N54-C21)	123.762	124.209	124.201	-0.447	-0.439	0.9818
C3-N53-C30 (C13-N54-C45)	118.413	117.639	117.939	0.775	0.475	0.6127
			dihedral angle			
C1-C2-C14-C15	24.174	18.516	19.082	5.658	5.092	0.8999
C3-N53-N54-C13	16.170	12.260	12.365	3.911	3.805	0.9729
C3-N53-C30-C31 (C13-N54-C45-C44)	87.926	87.911	87.993	0.015	-0.067	-4.3806

Table S2. The structural parameter with optimized structures for each state. Calculated using TD-DFT for S_1 state and DFT for S_0 and T_1 state with B3LYP/6-31g(d,p). Solvent effect was taken into account using PCM for DCM.

B3LYP/6-31g(d,p)	S_0	S_1	T_1	$\Delta(S_1-S_0)$	$\Delta(T_1-S_0)$	$\Delta(T_1-S_0)/\Delta(S_1-S_0)$
			bond length			
B52-C2 (B52-C14)	1.5476	1.5392	1.5438	0.0084	0.0038	0.449
B52-C26	1.5162	1.5343	1.5178	-0.0181	-0.0016	0.087
N53-C3 (N54-C13)	1.4057	1.4212	1.4169	-0.0155	-0.0112	0.721
N53-C25 (N54-C21)	1.4024	1.3941	1.4011	0.0083	0.0013	0.156
C2-C3 (C13-C14)	1.4257	1.4386	1.4391	-0.0129	-0.0134	1.038
C25-C26 (C21-C26)	1.4247	1.4101	1.4183	0.0146	0.0065	0.441
N54-C45 (N53-C30)	1.4442	1.4465	1.4467	-0.0023	-0.0025	1.099
C1-C15	3.3297	3.3610	3.3649	-0.0313	-0.0352	1.125
			angle			
C2-B52-C14	129.178	129.802	129.610	-0.623	-0.432	0.693
C2-B52-C26 (C14-B52-C26)	115.410	115.099	115.195	0.311	0.215	0.693
C3-N53-C25 (C13-N54-C21)	123.712	124.223	124.143	-0.510	-0.431	0.844
C3-N53-C30 (C13-N54-C45)	118.422	117.673	117.894	0.749	0.528	0.706
			dihedral angle			
C1-C2-C14-C15	22.341	17.185	17.181	5.156	5.160	1.001
C3-N53-N54-C13	14.870	11.266	11.114	3.604	3.756	1.042
C3-N53-C30-C31 (C13-N54-C45-C44)	87.884	87.857	88.072	0.027	-0.188	-6.854

Table S3. The structural parameter with optimized structures for each state. Calculated using TD-DFT for S_1 state and DFT for S_0 and T_1 state with BMK/6-31g(d,p). Solvent effect was taken into account using PCM for DCM.

BMK/6-31g(d,p)	S_0	S_1	T_1	$\Delta(S_1-S_0)$	$\Delta(T_1-S_0)$	$\Delta(T_1-S_0)/\Delta(S_1-S_0)$
			bond length			
B52-C2 (B52-C14)	1.5398	1.5343	1.5351	0.0055	0.0047	0.8517
B52-C26	1.5086	1.5148	1.5090	-0.0061	-0.0003	0.0506
N53-C3 (N54-C13)	1.3996	1.4062	1.4138	-0.0066	-0.0142	2.1548
N53-C25 (N54-C21)	1.3956	1.3942	1.3911	0.0014	0.0045	3.1761
C2-C3 (C13-C14)	1.4286	1.4451	1.4427	-0.0165	-0.0140	0.8503
C25-C26 (C21-C26)	1.4295	1.4190	1.4230	0.0105	0.0065	0.6210
N54-C45 (N53-C30)	1.4393	1.4415	1.4417	-0.0021	-0.0024	1.1268
C1-C15	3.3183	3.3455	3.3534	-0.0272	-0.0350	1.2894
			angle			
C2-B52-C14	129.050	129.299	129.531	-0.248	-0.481	1.936
C2-B52-C26 (C14-B52-C26)	115.475	115.351	115.234	0.124	0.240	1.936
C3-N53-C25 (C13-N54-C21)	123.853	124.534	124.217	-0.681	-0.364	0.534
C3-N53-C30 (C13-N54-C45)	118.384	117.691	117.734	0.694	0.650	0.937
			dihedral angle			
C1-C2-C14-C15	22.909	19.013	18.322	3.896	4.587	1.177
C3-N53-N54-C13	14.928	12.010	11.816	2.918	3.113	1.067
C3-N53-C30-C31 (C13-N54-C45-C44)	87.696	87.499	87.874	0.197	-0.178	-0.901

Table S4. The structural parameter with optimized structures for each state. Calculated using TD-DFT for S_1 state and DFT for S_0 and T_1 state with M062X/6-31g(d,p). Solvent effect was taken into account using PCM for DCM.

M062X/6-31g(d,p)	S_0	S_1	T_1	$\Delta(S_1-S_0)$	$\Delta(T_1-S_0)$	$\Delta(T_1-S_0)/\Delta(S_1-S_0)$
			bond length			
B52-C2 (B52-C14)	1.5459	1.5425	1.5434	0.0034	0.0025	0.7337
B52-C26	1.5152	1.5148	1.5137	0.0004	0.0015	3.5952
N53-C3 (N54-C13)	1.4000	1.4039	1.4175	-0.0039	-0.0175	4.5026
N53-C25 (N54-C21)	1.3955	1.3949	1.3876	0.0006	0.0079	12.3281
C2-C3 (C13-C14)	1.4180	1.4349	1.4307	-0.0169	-0.0126	0.7478
C25-C26 (C21-C26)	1.4185	1.4114	1.4131	0.0071	0.0053	0.7567
N54-C45 (N53-C30)	1.4372	1.4398	1.4399	-0.0026	-0.0027	1.0227
C1-C15	3.3223	3.3561	3.3698	-0.0338	-0.0475	1.4054
			angle			
C2-B52-C14	129.120	129.313	129.791	-0.193	-0.671	3.481
C2-B52-C26 (C14-B52-C26)	115.440	115.344	115.105	0.096	0.336	3.480
C3-N53-C25 (C13-N54-C21)	124.020	124.864	124.406	-0.844	-0.387	0.458
C3-N53-C30 (C13-N54-C45)	118.262	117.584	117.557	0.678	0.705	1.039
			dihedral angle			
C1-C2-C14-C15	23.193	18.991	17.909	4.202	5.284	1.257
C3-N53-N54-C13	15.135	11.538	11.475	3.597	3.660	1.017
C3-N53-C30-C31 (C13-N54-C45-C44)	87.113	87.192	87.687	-0.079	-0.574	7.259

Figure S1-S9

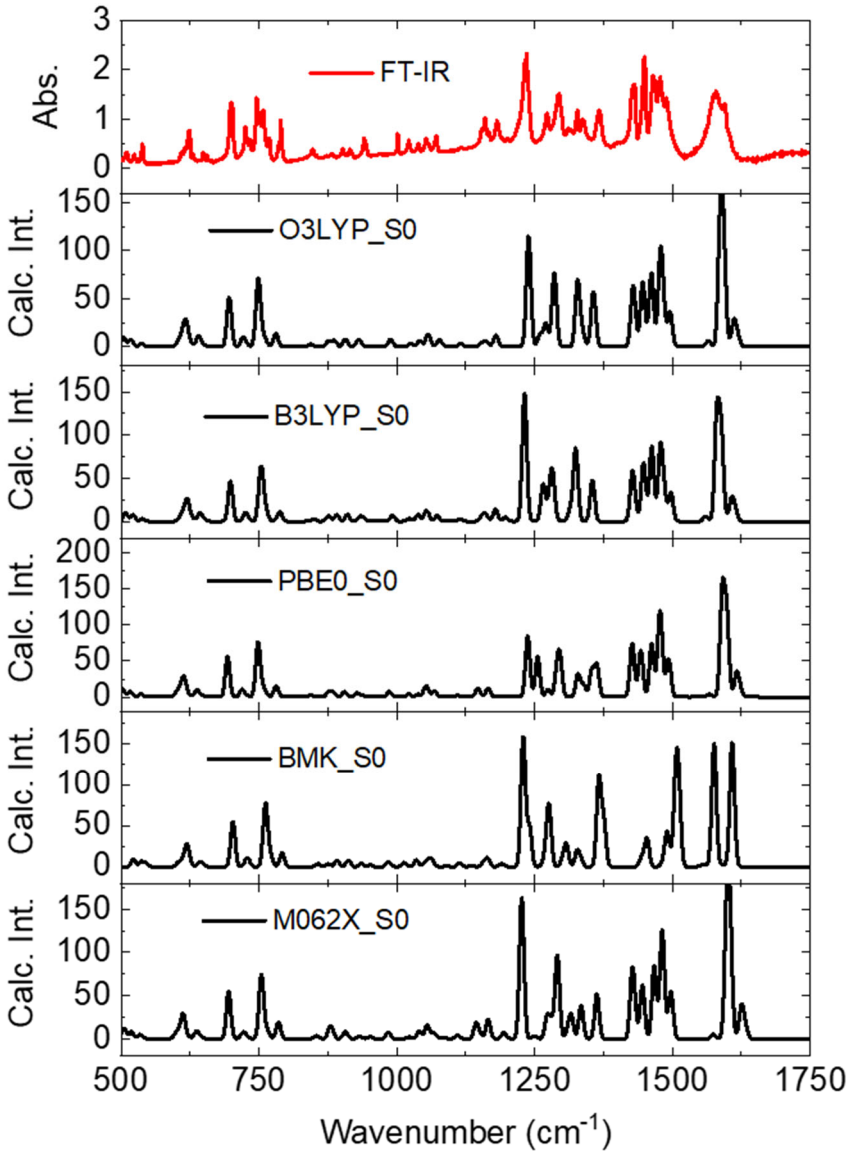

Figure S1. Comparison of FT-IR spectrum (red) and calculated spectra (black). FT-IR spectrum was measured with KBr pellet. Calculated spectra were obtained with optimized structure by each functional. The scaling factors of 0.975, 0.970, 0.965, 0.980, and 0.965 were adopted for B3LYP, BMK, M062X, O3LYP, and PBE0 functionals, respectively.

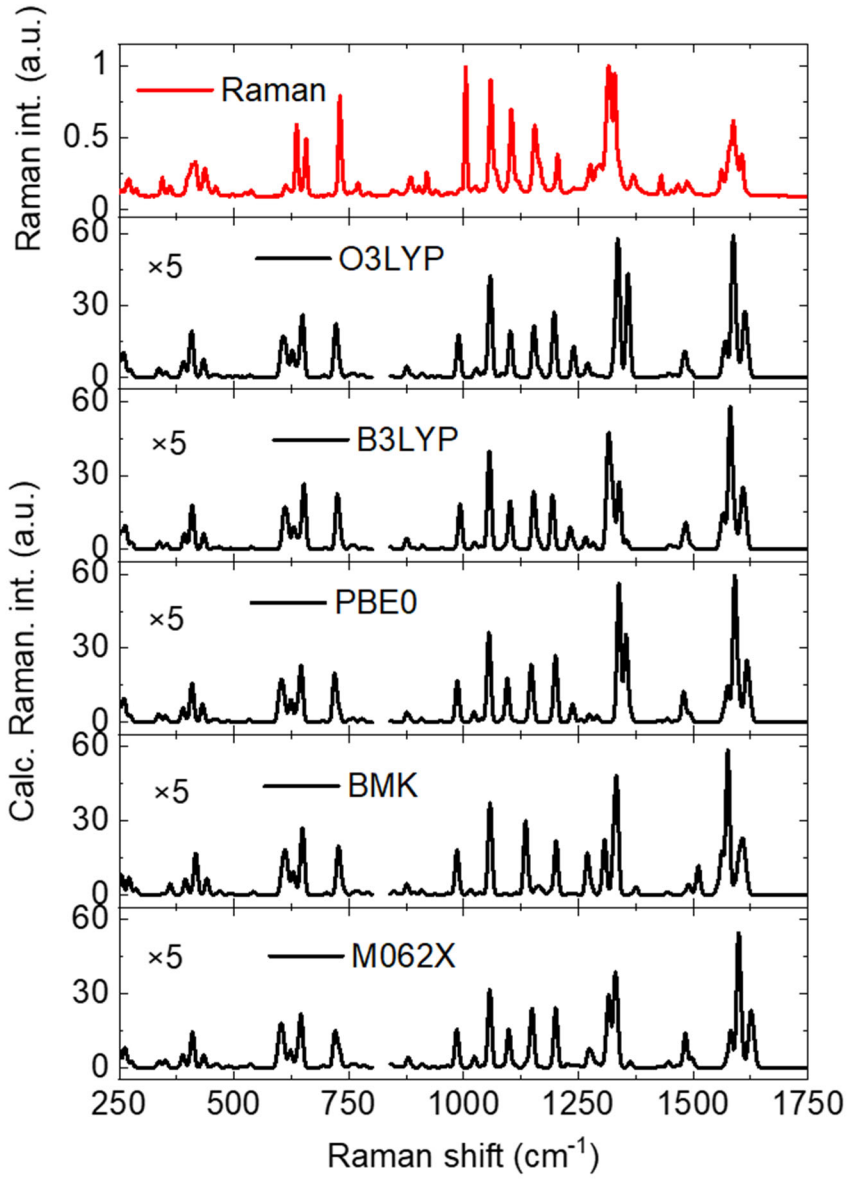

Figure S2. Comparison of Raman spectrum (red) and calculated spectra (black). Raman spectrum was measured with powder samples. Calculated spectra were obtained with optimized structure by each functional. The scaling factors of 0.975, 0.970, 0.965, 0.980, and 0.965 were adopted for B3LYP, BMK, M062X, O3LYP, and PBE0 functionals, respectively. For calculated spectra, the regions below 800 cm^{-1} were multiplied by 5 for visibility.

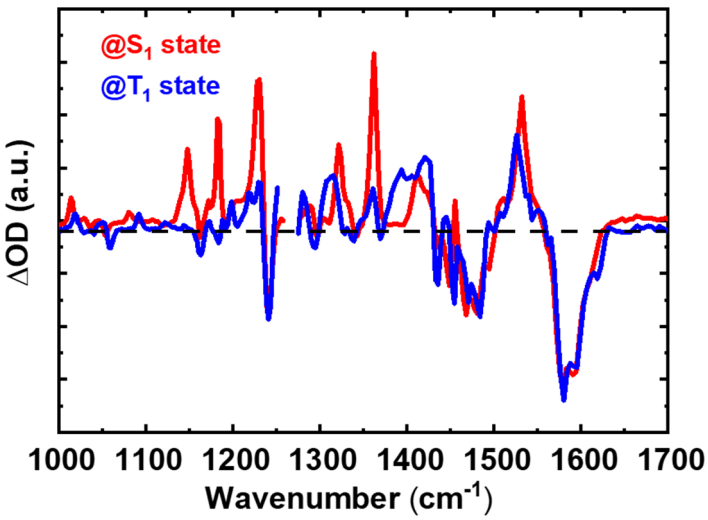

Figure S3. Comparison of TR-IR spectra at S_1 and T_1 states. The spectrum at S_1 and T_1 states was recorded at 1 ns and 50 ns after photoexcitation with 440 nm, respectively.

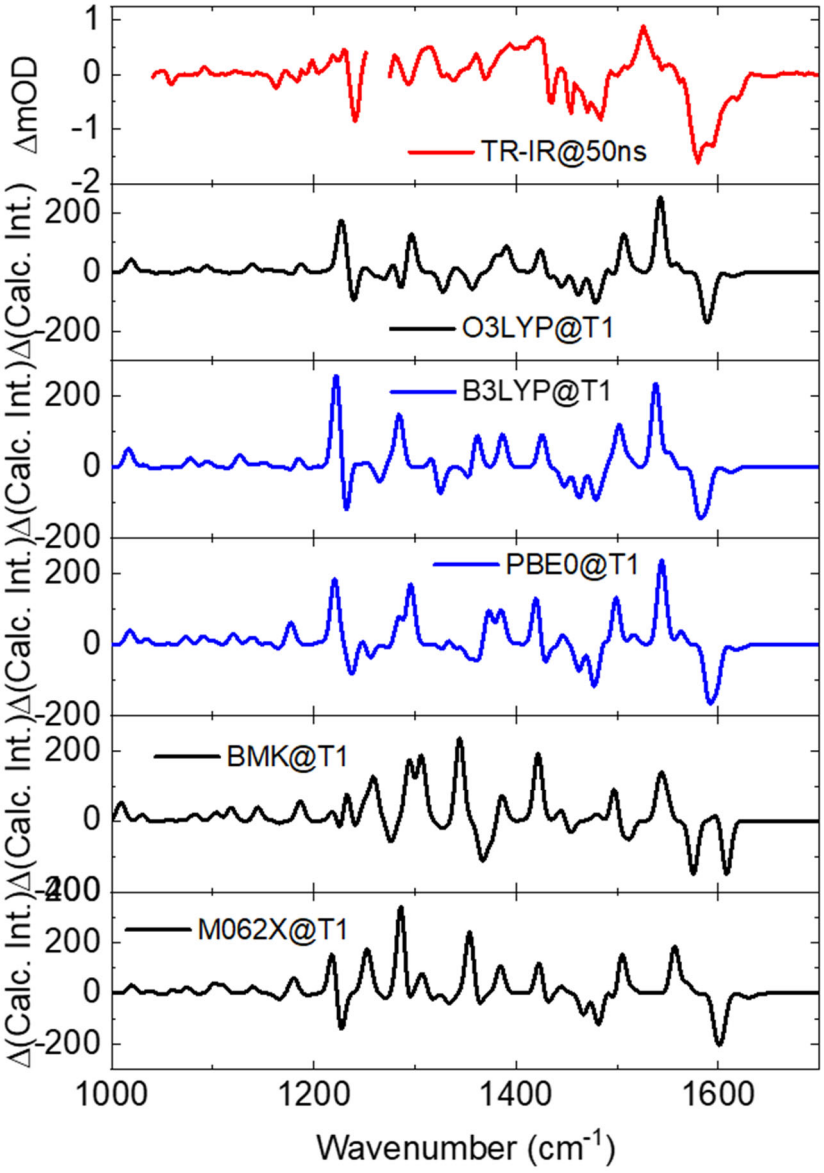

Figure S4. Dependence on the choice of functional for calculated spectrum in T_1 state. The basis set was 6-31g(d,p) in each case. Solvent effect was taken into account using PCM for DCM.

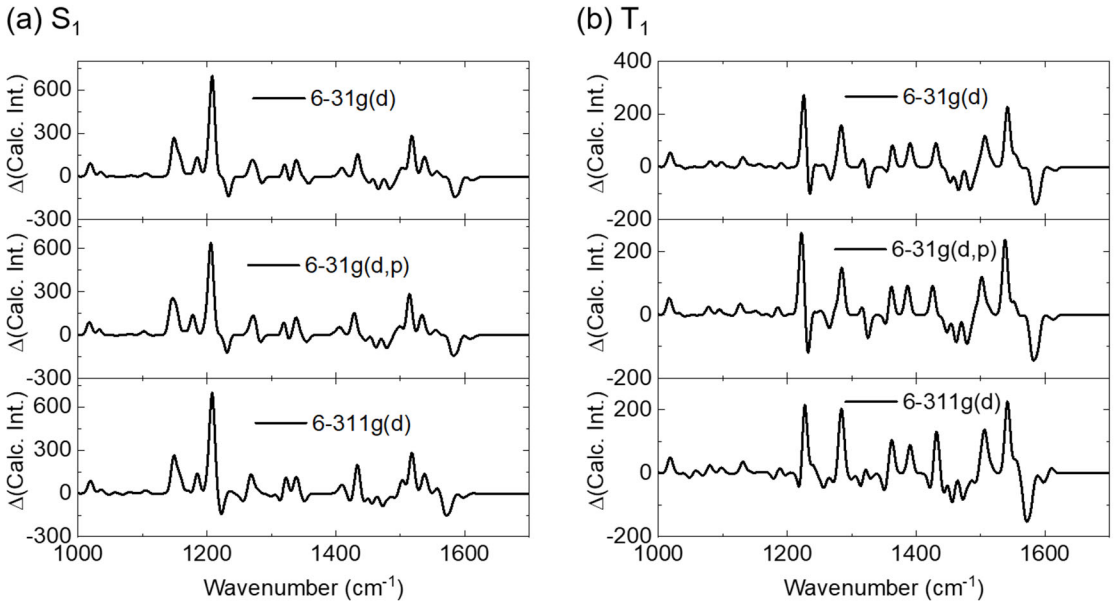

Figure S5. Dependence on the choice of basis set for calculated spectrum in (a) S_1 and (b) T_1 state. The B3LYP functional was used in each case. Solvent effect was taken into account using PCM for DCM.

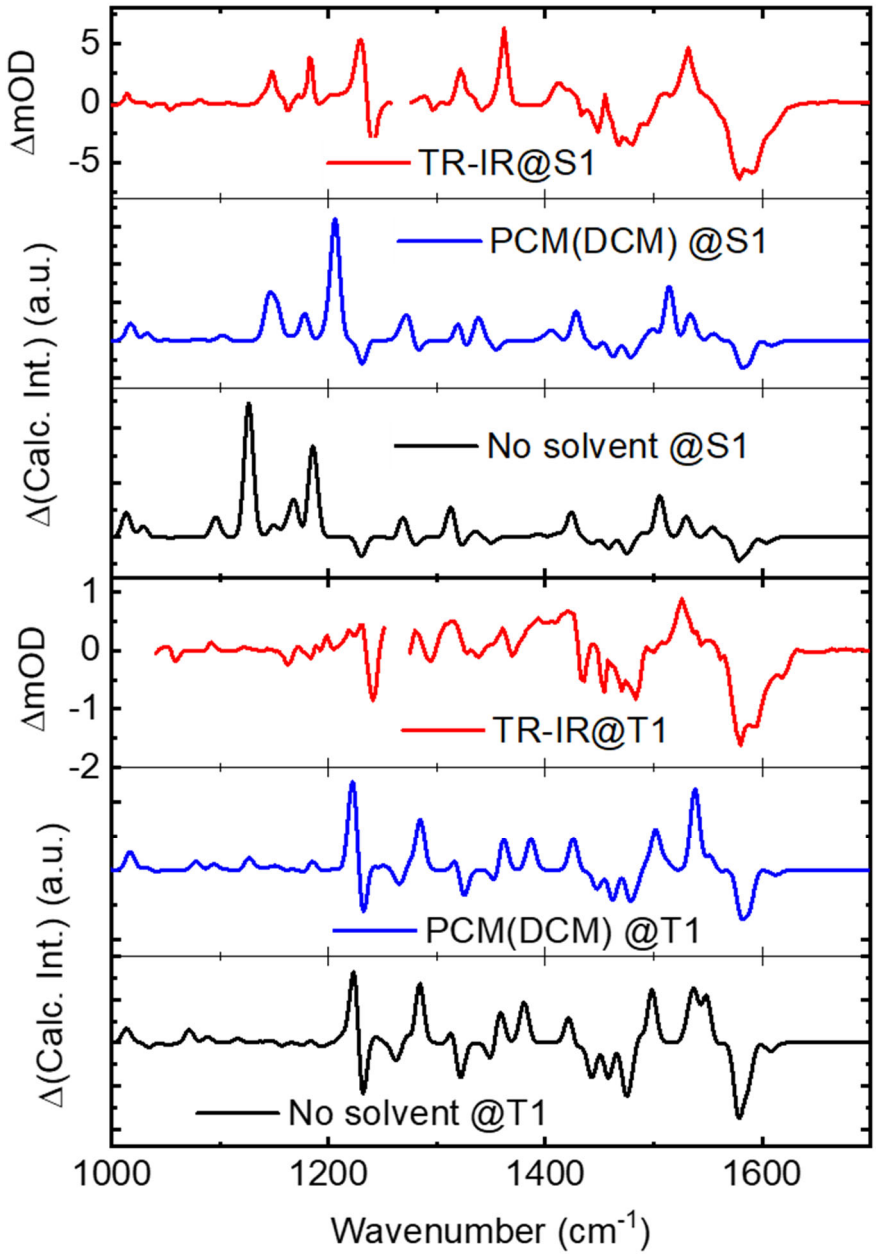

Figure S6. Dependence on the presence(blue)/absence(black) of solvent effects for S_1 (upper) and T_1 state (lower) in the quantum chemical calculations. The functional and basis set was B3LYP/6-31G(d,p) in each case. We tested the solvent effects of using the PCM of the solvent DCM. TR-IR spectra are shown in red for comparison.

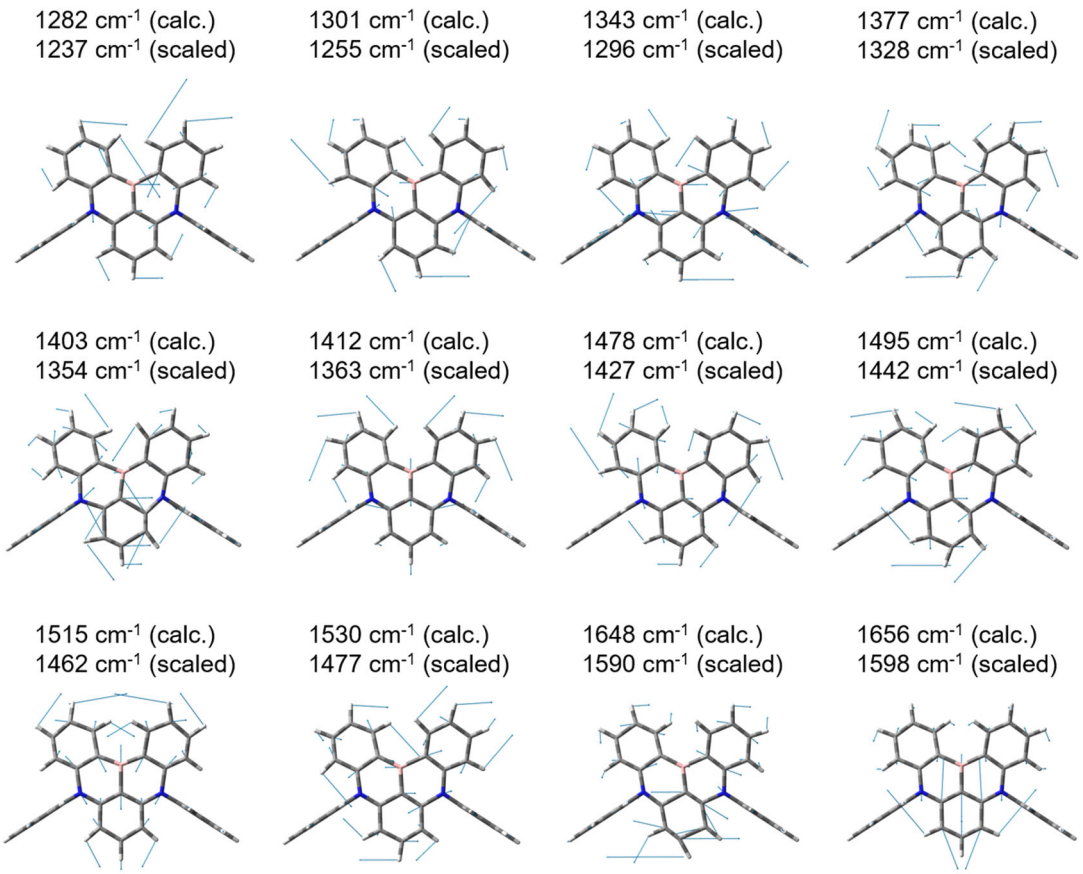

Figure S7. Vibrational assignment of **DABNA-1** in S_0 state. Calculated with PBE0/6-31g(d,p) level. Solvent effect was taken into account using PCM for DCM. The scaling factors of 0.965 were adopted.

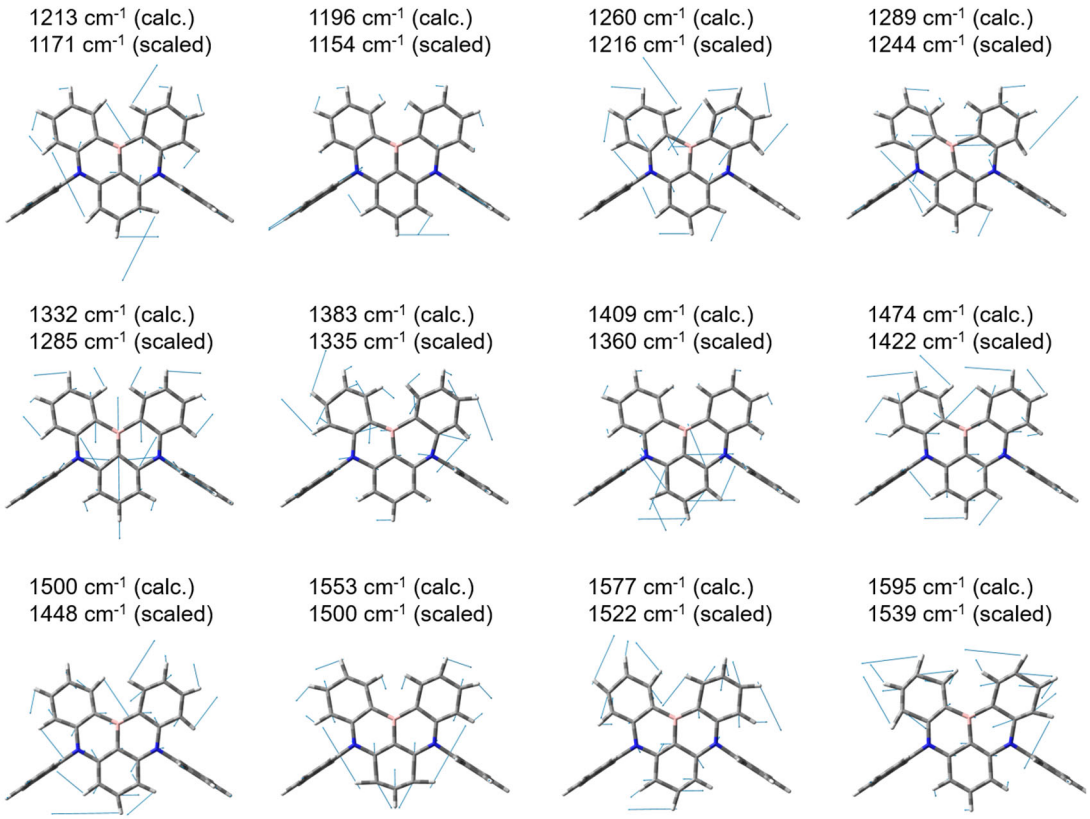

Figure S8. Vibrational assignment of **DABNA-1** in S_1 state. Calculated with TD-PBE0/6-31g(d,p) level. Solvent effect was taken into account using PCM for DCM. The scaling factors of 0.965 were adopted.

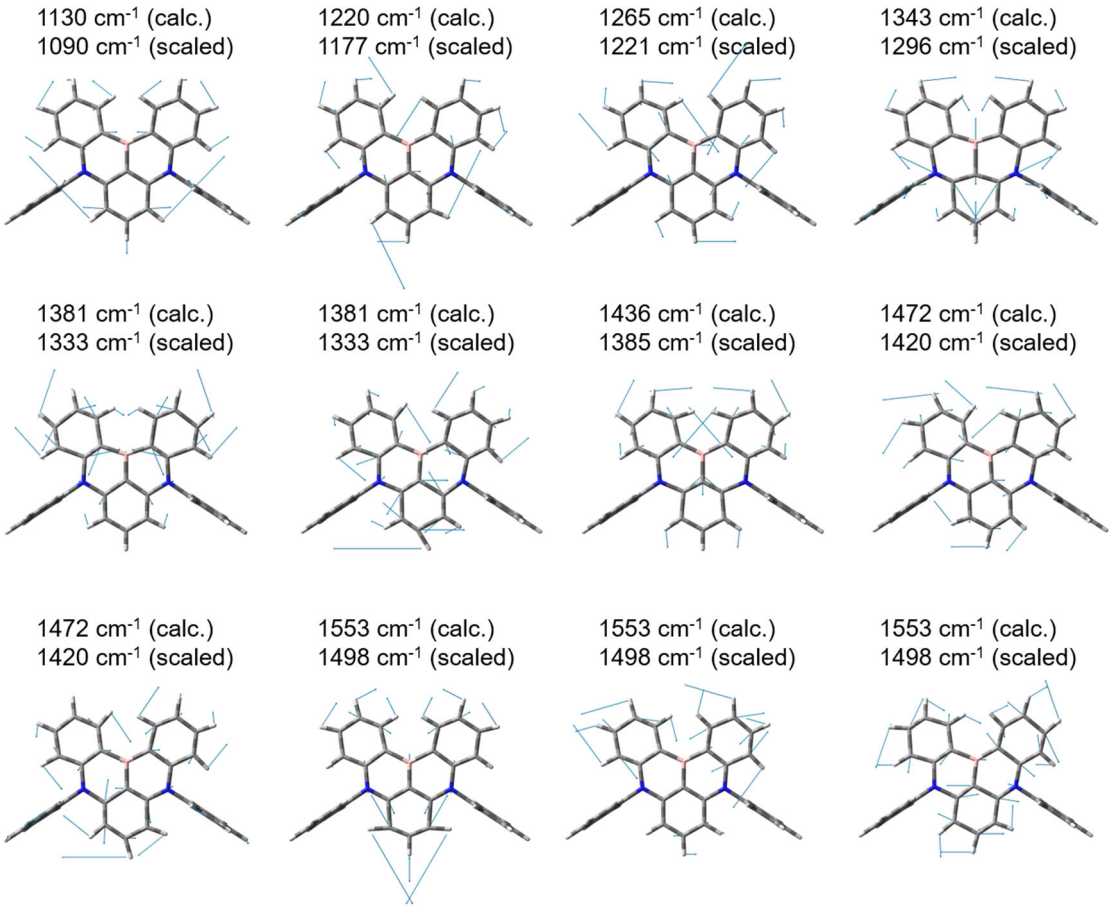

Figure S9. Vibrational assignment of **DABNA-1** in T_1 state. Calculated with PBE0/6-31g(d,p) level. Solvent effect was taken into account using PCM for DCM. The scaling factors of 0.965 were adopted.